Electronic structure of ferromagnetic semiconductor $CrGeTe_3$ by angle-resolved photoemission spectroscopy

Y. F. Li,[1] W. Wang,[2] W. Guo,[1] C. Y. Gu,[1] H. Y. Sun,[1] L. He,[2] J. Zhou,[1] Z. B. Gu,[1] Y. F. Nie,[1,*] and X. Q. Pan[1,3]

[1]*National Laboratory of Solid State Microstructures, College of Engineering and Applied Sciences, and Collaborative Innovation Center of Advanced Microstructures, Nanjing University, Nanjing 210093, China*

[2]*Jiangsu Provincial Key Laboratory of Advanced Photonic and Electronic Materials, Collaborative Innovation Center of Advanced Microstructures, School of Electronic Science and Engineering, Nanjing University, Nanjing 210093, China*

[3]*Department of Chemical Engineering and Materials Science and Department of Physics and Astronomy, University of California, Irvine, 916 Engineering Tower, Irvine, California 92697, USA*

(Received 26 April 2018; revised manuscript received 3 August 2018; published 14 September 2018)

As one of the rare ferromagnetic semiconductors, $CrGeTe_3$ has recently attracted a great deal of attention as a potential candidate for next-generation high-performance nano-spintronic devices. In this study, by combining density functional theory calculations and angle-resolved photoemission spectroscopy measurements, we explore the electronic structure of $CrGeTe_3$ directly. The low-lying valence bands are centered around the Γ point and mainly consist of Te $5p$ orbitals. The majority of the bands show almost no k_z dispersion, consistent with its layered crystalline structure. Due to the higher hopping integral along the out-of-plane direction, however, bands comprised of p_z orbitals exhibit significant k_z dispersion. Furthermore, an indirect band gap of 0.38 eV is directly measured by surface electron doping with potassium deposition.

DOI: 10.1103/PhysRevB.98.125127

I. INTRODUCTION

Since the successful exfoliation of graphene [1], novel and compelling phenomena in reduced dimensional systems have attracted a great deal of attention not only for their revelation about fundamental physics [2,3], but also because they are promising candidates for next-generation electronic devices. Unfortunately, the fact that graphene has no band gap imposes large restrictions on its potential applications [4]. Consequently, attention has been extended to quasi-two-dimensional semiconductors, such as the monolayer of hexagonal boron nitride (*h*-BN) [5,6] and transition-metal dichalcogenides (TMDs) [7–10].

Recently, $CrGeTe_3$ and its analog $CrSiTe_3$ have attracted attention as potential candidates for high-performance nano-spintronics because they display an inherent ferromagnetic property and a semiconductor characteristic simultaneously [11–14]. From a theoretical standpoint, the phonon spectrum and the electronic structure of $CrSiTe_3$ have been studied by density functional theory (DFT) calculations [15–17]. Moreover, their ferromagnetic phase transition has been predicted through simulation calculations by adopting various models, including the three-dimensional (3D) Ising model, the 3D Heisenberg model, and tricritical mean-field theory [18–21]. To achieve a magnetic property in many nonmagnetic materials, subtle regulations are required by edge [22], strain engineering [23], or electron-hole pair resonance [24]. However, an inherent ferromagnetism of $CrGeTe_3$ and $CrSiTe_3$ both in bulk form and monolayer form has been proposed to be a competing behavior where the ferromagnetism derives from the superexchange interaction of Cr-Te-Cr structure but mediated by the exchange interactions of t_{2g} orbitals of neighboring high-spin Cr^{3+} ions [13,25–27]. Meanwhile, from an experimental point of view, there have been studies on the temperature-dependent magnetization and specific heat, revealing a ferromagnetic phase transition for $CrGeTe_3$ and $CrSiTe_3$ with a Curie temperature of 67 and 32 K, respectively [13,16,17,20,25]. Direct observation of spin waves of $CrSiTe_3$ has also been reported in a previous work [27], and optical property measurements indicate a direct band gap of 1.2 eV and an indirect gap of 0.4 eV for $CrSiTe_3$ [13,25]. However, investigations on the electronic property of $CrGeTe_3$ have been comparatively limited, but in fact it displays more promising properties for application due to its higher Curie temperature and conductivity compared with $CrSiTe_3$. A direct measurement on the electronic structure will provide important information on the property of electrons and will offer guidance regarding the design and fabrication of related electronic devices.

In this work, by combining DFT calculations with angle-resolved photoemission spectroscopy (ARPES) measurements, we explore the electronic structure of $CrGeTe_3$ directly. Our results show that the low-lying valence bands are centered around the Γ point and are mainly comprised of Te $5p$ orbitals. Due to the various space orientations and integral of p orbitals, two sets of electron bands dominated by different p orbitals display different k_z dispersions and effective mass, which is also confirmed by ARPES measurements. By *in situ* K doping, we observe the bottom of the conduction band below the Fermi level, with an indirect band gap of 0.38 eV.

*ynie@nju.edu.cn

II. EXPERIMENTAL DETAILS

High-quality $CrGeTe_3$ single crystal is synthesized from elemental Cr(99.99%), Ge(99.99%), and Te(>99.999%) materials with high purity (ordered from *Alfa Aesar*). A mixture of materials with an optimized ratio of Cr:Ge:Te equivalent to 10:13.5:76.5 is sealed in evacuated quartz ampoules and heated at 1050 °C for 1 day, followed by slow cooling to 450 °C for a period of 7 days. Magnetism measurements are performed on the SQUID-VSM system.

As the Te $5p$ states and the majority spin of Cr $3d$ states predominately contribute to the density of states near the valence-band top and conduction-band bottom, for accurate treatment with the localized $3d$ orbitals with strong correlation, DFT calculations are performed under the framework of the Heyd-Scuseria-Ernzerhof (HSE06) hybrid density functional implemented in the Vienna *ab initio* simulation package (VASP). In addition, van der Waals interactions have a significant impact on the layered structure of $CrGeTe_3$ and $CrSiTe_3$, and consequently affect the bulk band structure. After comparing different van der Waals functions (Table I) [28,29], we adopt the Grimme (DFT-D2) method to deal with the van der Waals interactions. The lattice constants for $CrGeTe_3$ are optimized to be $a = b = 6.924$ Å, $c = 20.381$ Å, in agreement with the experimental value ($a = b = 6.820$ Å, $c = 20.371$ Å for $CrGeTe_3$).

For ARPES measurements, $CrGeTe_3$ and $CrSiTe_3$ crystals were cleaved *in situ* and under a vacuum base pressure better than 6×10^{-11} Torr. To avoid the charging effect, $CrGeTe_3$ and $CrSiTe_3$ were measured at 50 and 120 K, respectively. Incident uv light is generated from the characteristic radiation of He Iα and He IIα by a helium discharge lamp, with kinetic energy of 21.2 and 40.8 eV, respectively. *In situ* low-energy electron diffraction (LEED) measurements are conducted after ARPES measurements to confirm the surface condition throughout the measurements.

III. EXPERIMENTAL RESULTS AND DISCUSSION

The crystalline structure of $CrGeTe_3$ is shown in Fig. 1(a). As an emerging member of layered chalcogenide, $CrGeTe_3$ is comparatively rare in its germanium pairs forming $(Ge_2Te_6)^{6-}$ ethanelike groups. Located in the slightly distorted octahedral structure, Cr^{3+} ions and Ge-Ge pairs form a Te-(Cr,Ge-Ge)-Te sandwich layer in the ratio of 2:1 with triangular symmetry in-plane. Along the c axis, each unit cell is comprised of three $CrGeTe_3$ layers stacked in the ABC sequence. The fresh and flat surface of single crystal after exfoliation is shown in Fig. 1(b). In Fig. 1(d), 2Θ-ω x-ray diffraction (XRD) scans along the (00l) direction for $CrGeTe_3$ and $CrSiTe_3$ indicate high crystalline quality of the sample with no sign of impurity phases. As shown in the insets of Fig. 1(d), an azimuthal scan on the (116) peaks shows six peaks separated by 60°. To confirm the quality of the sample surface throughout our measurements, *in situ* LEED measurements are performed after the ARPES measurements and exhibit clear and sharp diffraction spots with low background [Fig. 1(c)], which indicate the fresh and high-quality surface with a minor amount of impurities or disorder. As is marked

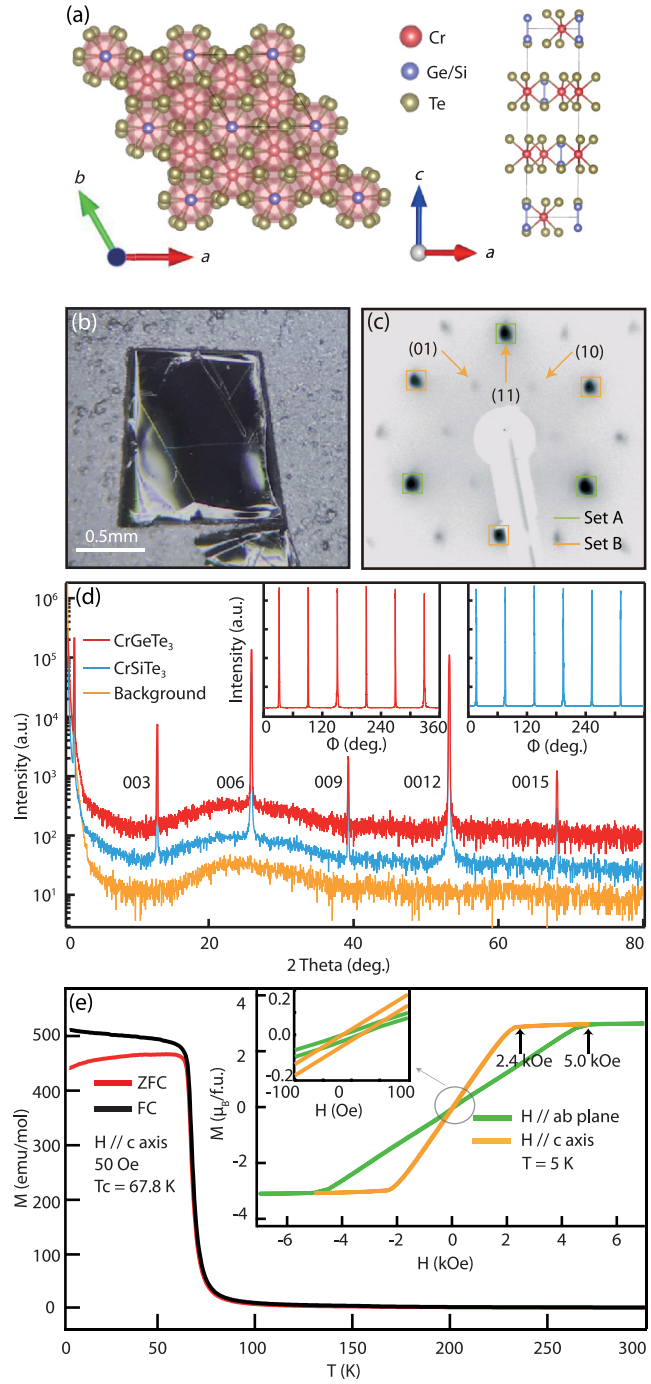

FIG. 1. (a) Schematic illustration of the crystalline structure of $CrGe(Si)Te_3$ from the top view and the side view. A unit cell is indicated by a black line. (b) Morphology of a fresh surface of $CrGeTe_3$ after exfoliation. (c) *In situ* LEED patterns after ARPES measurements to confirm the quality of the surface. The markers indicate two sets of (11) diffraction pattern. (d) 2Θ-ω x-ray diffraction scan along the (00l) direction. The insets show azimuthal Φ scans of (116) diffraction peaks for $CrGeTe_3$ and $CrSiTe_3$. (e) ZFC-FC curves with 50 Oe external magnetic field parallel to the c axis. The inset shows the isothermal magnetization curves $M(H)$ at 5 K. The saturation field is 5.0 kOe with an external field parallel to the ab plane (green line) and 2.4 kOe (orange line) parallel to the c axis. A zoom-in of the magnetization curve shows no significant coercive force.

TABLE I. Comparisons for different vdW corrections.

$CrGeTe_3$	Experimental value (5 K)	Original vdW of Dion	optPBE	optB88	optB88b
a	6.82	7.115	7.016	6.974	6.923
c	20.371	22.208	21.466	20.995	20.745
a%	0.00%	4.33%	2.87%	2.26%	1.51%
c%	0.00%	9.02%	5.38%	3.06%	1.84%
$CrGeTe_3$	Experimental value (5 K)	Grimme-D3 zero damping	D3 BJ damping	DF2	Grimme-D2
a	6.82	6.939	6.958	7.211	6.924
c	20.371	22.590	22.713	22.068	20.381
a%	0.00%	1.74%	2.02%	5.73%	1.52%
c%	0.00%	10.89%	11.50%	8.33%	0.05%

in Fig. 1(c), the (11) diffraction patterns are comprised of two sets of spots with an intensity ratio of 1.41:1, which corresponds to its triangular symmetry in-plane (Space Group No. 148, R-3) [17].

As shown in Fig. 1(e), zero-field-cooled (ZFC) and field-cooled (FC) magnetization measurements show a ferromagnetic phase transition at a critical point around 67.8 K, almost twice as large as that of $CrSiTe_3$, in agreement with previous reports [17,20,30,31]. The ferromagnetism in both systems originates from the near-90° Cr-Te-Cr superexchange interaction but mediated by the direct t_{2g}-t_{2g} interactions of high-spin Cr^{3+}. Apart from direct simulation calculations [16,19,26], the enhanced Curie temperature for $CrGeTe_3$ can be explained by the steric effect, where the much longer Ge_2 pairs in $CrGeTe_3$ lead to (i) a comparatively larger bond length for Cr-Cr (0.3942 nm for $CrGeTe_3$ and 0.3909 nm for $CrSiTe_3$), and (ii) the Cr-Te-Cr bond angle closer to 90° (90.4° for $CrGeTe_3$ and 91.6° for $CrSiTe_3$) [17]. This structural effect contributes to an enhanced Curie temperature for $CrGeTe_3$ compared with $CrSiTe_3$. The inset of Fig. 1(d) illustrates a typical ferromagnetic behavior with no significant coercive force, and magnetic saturation is achieved at 5 kOe (with external magnetic field parallel to *ab* plane) and 2.4 kOe (with external magnetic field along the *c* axis). The anisotropy suggests the crystallographic *c*-axis is comparatively easier to be magnetized. Parallel to the *c* axis, the effective moment is $3.94\mu_B$, corresponding well with the expected value of $3.87\mu_B$ that originated from the three unpaired spins of Cr^{3+} ions.

The band structure along the path Γ-*M*-*K*-Γ-*A* [as illustrated in Fig. 2(a)] and the density of states calculated by the aforementioned DFT settings are shown in Fig. 2(b). The

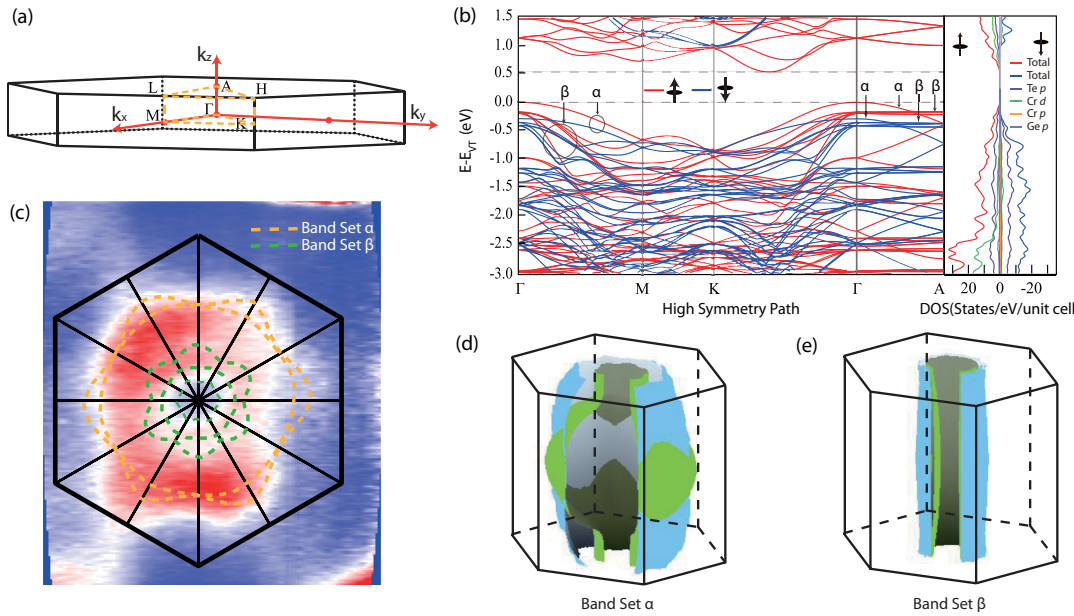

FIG. 2. (a) The Brillouin zone of $CrGeTe_3$ and the high-symmetry path. (b) Calculated band structures along the high-symmetry path and total and projected density of states for spin-up and spin-down states. E_F is aligned with the valence-band top. (c) ARPES isoenergy mapping in the first Brillouin zone with binding energy of 0.7 eV. The orange dashed lines are the corresponding energy contour for band set α and the green dashed lines for band set β. Calculated isoenergy surface for (d) band set α and (e) band set β with corresponding binding energy of ARPES mapping. (The Brillouin zone has been expanded threefold along the k_z axis for better illustration.)

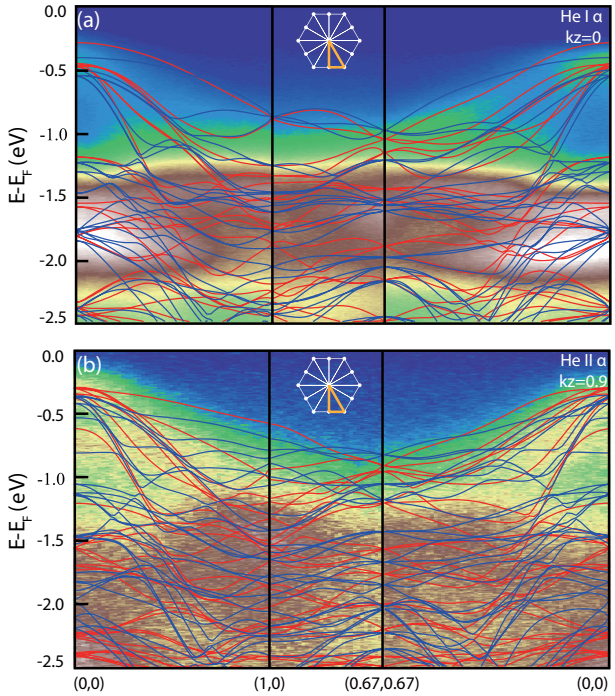

FIG. 3. ARPES spectra along the path of (0,0)-(1,0)-(0.67,0.67)-(0,0) taken with (a) He Iα and (b) He IIα photons. The calculated band dispersion is superimposed. Schematic illustration of the high-symmetry path in the first Brillouin zone is shown in the inset.

valence-band top is centered around the Γ point, and the conduction-band bottom is lying between Γ-K, showing an indirect band gap of 0.53 eV. After projecting the density of states on specific orbitals, Te $5p$ orbitals dominate the states near the valence-band top and Cr $3d$ orbitals dominate the conduction-band bottom. As is shown in Fig. 2(b), there are multiple low-lying valence bands with similar binding energy and they can be categorized into two sets of bands (α and β) for the comparison with ARPES data. Band sets α and β exhibit distinct dispersions along the k_z direction. The isoenergy surface with a binding energy of 0.7 eV for band set β [in Fig. 2(e)] is cylindrical, corresponding to the characteristic of two-dimensional materials, whereas for band set α its isoenergy surface [in Fig. 2(d)] is strongly warped cylindrical, indicating its significant k_z dispersion. Considering the fact that band set α is predominantly comprised of Te $5p_z$ orbitals, such k_z dispersion can be attributed to the higher hopping integral along the out-of-plane direction. For band set β, however, Te $5p_x$ and Te $5p_y$ orbitals dominate, so no apparent k_z dispersion is observed and the electrons are mainly confined in-plane.

The ARPES isoenergy mapping with a binding energy of 0.7 eV is shown in Fig. 2(c). The general characteristic is in agreement with what DFT calculation predicts. Despite the fact that spectral intensity is strongly affected by the matrix element effect, the sixfold symmetry of the electronic structure of $CrGeTe_3$ can still be observed. The holelike state centered around the Γ point can be decomposed into an outer set and

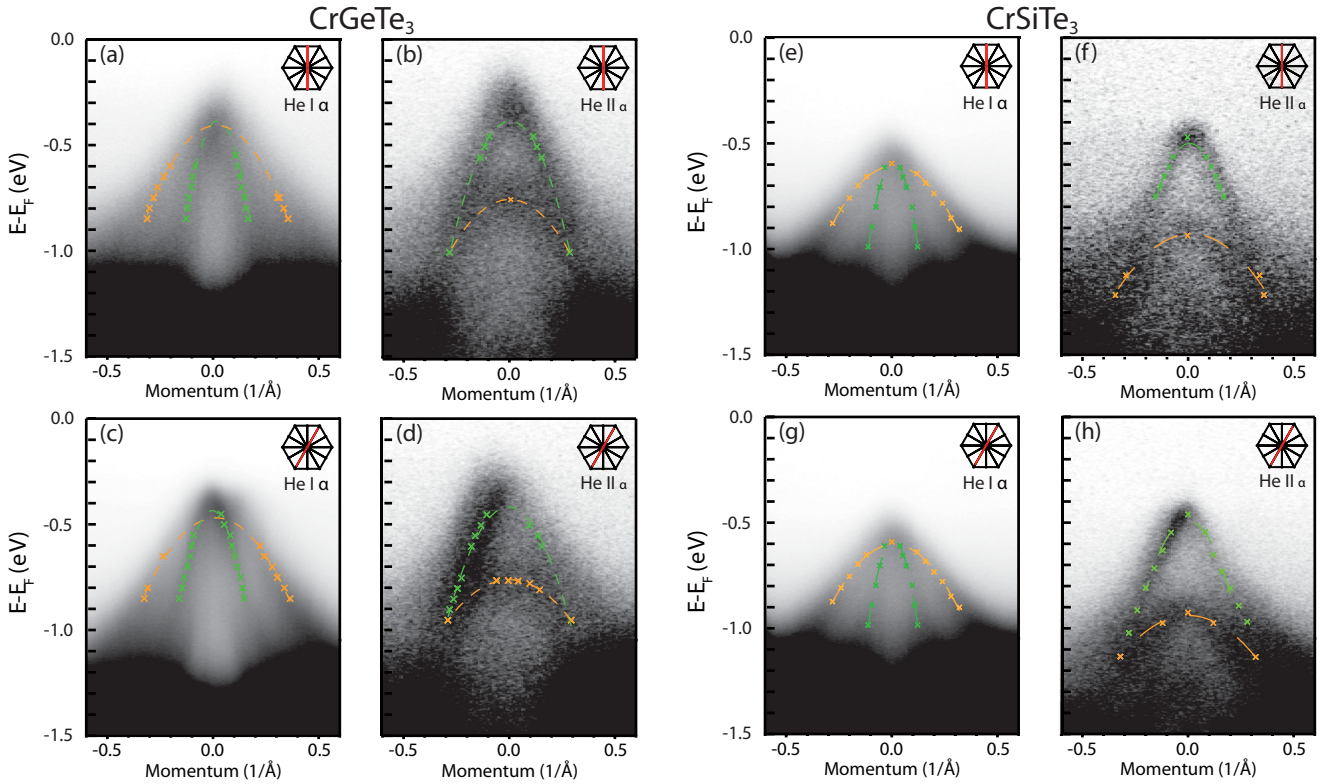

FIG. 4. Detailed structure of valence bands along the path of $(-1, 0)$-$(0, 0)$-$(1, 0)$ for $CrGeTe_3$ with (a) He Iα and (b) He IIα ARPES spectra. Detailed structure of valence band along the path of $(-0.67, -0.67)$-$(0, 0)$-$(0.67, 0.67)$ for (c) He Iα and (d) He IIα ARPES spectra. Parts (e)–(h) are the corresponding results for $CrSiTe_3$. Crossings are the fitting points. Band set α is denoted by an orange dashed line and band β by a green dashed line under parabola fitting.

an inner set, which are contributed by band set α and band set β, respectively. Two orange dashed lines in Fig. 2(c) are the calculated isoenergy contour with corresponding binding energy for band set α, and the green dashed lines are for band set β.

ARPES spectra along the high-symmetry path are shown in Fig. 3. Due to the existence of a large number of bands, ARPES spectra are intrinsically broad, but qualitatively agree with DFT calculations. A slightly more clear and dispersive feature can be seen for the states near the Fermi level. The most distinct difference between the spectra taken by He Iα and He IIα photons is the extra band with a kinetic binding energy of about 0.7 eV near the Γ point only shown in He IIα spectra. By comparing experimental data with theoretical results, we can roughly estimate the k_z value of the spectra taken by He Iα and He IIα to be 0 and 0.9 (in units of π/c), respectively.

The detailed ARPES spectra of the band top along the Γ-centered path is shown in Fig. 4. Consistent with the theoretical calculations, the tops of the valence bands are comprised of two band sets (α and β), which are denoted by an orange dashed line and a green dashed line, respectively. ARPES spectra taken by He Iα photons are estimated to be at the k_z value of 0, and the average effective mass for holes in-plane are evaluated. Along the path of (0,0)-(0.5,0), the average effective mass is fitted to be $0.98(\pm0.05)m_e$ for band set α and $0.18(\pm0.01)m_e$ for band set β. As for the direction of (0,0)-(0.67,0.67), the effective mass is $0.86(\pm0.05)m_e$ for band set α and $0.22(\pm0.01)m_e$ for band set β, comparatively smaller than DFT calculation results. For $CrSiTe_3$, the average effective mass is fitted to be $1.09(\pm0.06)m_e$ and $0.12(\pm0.01)m_e$ along (0,0)-(0.5,0); and $0.96(\pm0.04)m_e$ and $0.15(\pm0.01)m_e$ along (0,0)-(0.67,0.67) for band sets α and β. By changing the incident photon from He Iα to He IIα, we observe a significant shift for band set α but no apparent shift for band set β (similar results have also been observed for $CrSiTe_3$), in good agreement with the different dispersion behavior along Γ-A in DFT calculation results [Fig. 2(b)].

By *in situ* K doping on the sample surface, the valence bands shift to higher binding energy as deposited K atoms donate electrons to the system. For $CrGeTe_3$, the bottom of the conduction band appears along the path of (0,0)-(0.67,0.67), consistent with DFT calculations. The band gap is 0.38 eV, as estimated from the ARPES He Iα spectrum ($k_z \approx 0$) shown in Fig. 5(a). We also tried *in situ* potassium doping for $CrSiTe_3$, but we could not observe the conduction band within the doping limit. This is consistent with the theoretical calculations, where the band gap for $CrSiTe_3$ is 0.67 eV, larger than $CrGeTe_3$ (0.53 eV).

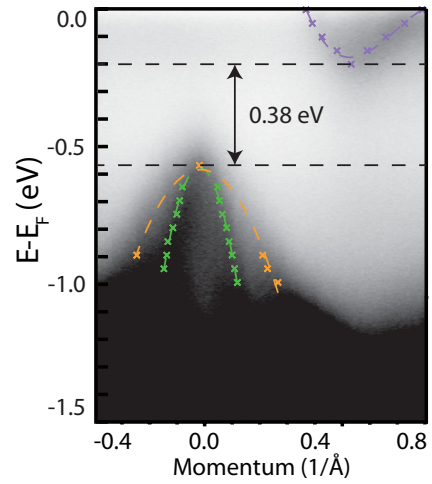

FIG. 5. The conduction band along the path of (0,0)-(0.67,0.67); band sets α and β are denoted by an orange dashed line and a green dashed line, respectively. The conduction band is denoted by a purple dashed line.

IV. CONCLUSION

In conclusion, by combining DFT calculations and ARPES measurements, we map out the electronic structure of the ferromagnetic semiconductor $CrGeTe_3$ directly. The valence-band top is centered around the Γ point, comprised of band set α and band set β with distinct k_z dispersion, which can be attributed to different orbital characters and integrals between layers. An indirect band gap of 0.38 eV is observed by K surface doping.

ACKNOWLEDGMENTS

This work is supported by the National Basic Research Programme of China (Grant No. 2015CB654901), the National Natural Science Foundation of China (Grants No. 11774153, No. 51672125, No. 11574135, No. 61474061, and No. 61674079), and the Fundamental Research Funds for the Central Universities (No. 0213-14380058). Y.F.N. is supported by National Thousand-Young-Talents Program and Program for High-Level Entrepreneurial and Innovative Talents Introduction. For DFT calculation, the authors acknowledge the use of the computational resources in the High-Performance Computing Center of Nanjing University. The authors also acknowledge Z.Y. Li for help with manuscript revision.

Y.F.L. and W.W. contributed equally to this work.

[1] A. K. Geim and K. S. Novoselov, Nat. Mater. **6**, 183 (2007).

[2] K. S. Novoselov, Z. Jiang, Y. Zhang, S. Morozov, H. L. Stormer, U. Zeitler, J. Maan, G. Boebinger, P. Kim, and A. K. Geim, Science **315**, 1379 (2007).

[3] K. S. Novoselov, A. K. Geim, S. Morozov, D. Jiang, M. Katsnelson, I. Grigorieva, S. Dubonos, and A. A. Firsov, Nature (London) **438**, 197 (2005).

[4] S. Stankovich, D. A. Dikin, G. H. Dommett, K. M. Kohlhaas, E. J. Zimney, E. A. Stach, R. D. Piner, S. T. Nguyen, and R. S. Ruoff, Nature (London) **442**, 282 (2006).

[5] K. Watanabe, T. Taniguchi, and H. Kanda, Nat. Mater. **3**, 404 (2004).

[6] G. Giovannetti, P. A. Khomyakov, G. Brocks, P. J. Kelly, and J. van den Brink, Phys. Rev. B **76**, 073103 (2007).

[7] B. Radisavljevic, A. Radenovic, J. Brivio, I. V. Giacometti, and A. Kis, Nat. Nanotechnol. **6**, 147 (2011).
[8] H. S. Lee, S.-W. Min, Y.-G. Chang, M. K. Park, T. Nam, H. Kim, J. H. Kim, S. Ryu, and S. Im, Nano Lett. **12**, 3695 (2012).
[9] M. Shanmugam, T. Bansal, C. A. Durcan, and B. Yu, Appl. Phys. Lett. **100**, 153901 (2012).
[10] Z. Deng, C. Jin, Q. Liu, X. Wang, J. Zhu, S. Feng, L. Chen, R. Yu, C. Arguello, T. Goko *et al.*, Nat. Commun. **2**, 422 (2011).
[11] A. K. Geim and I. V. Grigorieva, Nature (London) **499**, 419 (2013).
[12] A. MacDonald, P. Schiffer, and N. Samarth, Nat. Mater. **4**, 195 (2005).
[13] B. Liu, Y. Zou, L. Zhang, S. Zhou, Z. Wang, W. Wang, Z. Qu, and Y. Zhang, Sci. Rep. **6**, 33873 (2016).
[14] I. Žutić, J. Fabian, and S. D. Sarma, Rev. Mod. Phys. **76**, 323 (2004).
[15] B. Siberchicot, S. Jobic, V. Carteaux, P. Gressier, and G. Ouvrard, J. Phys. Chem. **100**, 5863 (1996).
[16] X. Li and J. Yang, J. Mater. Chem. C **2**, 7071 (2014).
[17] V. Carteaux, D. Brunet, G. Ouvrard, and G. Andre, J. Phys.: Condens. Matter **7**, 69 (1995).
[18] S. Lebègue, T. Björkman, M. Klintenberg, R. M. Nieminen, and O. Eriksson, Phys. Rev. X **3**, 031002 (2013).
[19] M.-W. Lin, H. L. Zhuang, J. Yan, T. Z. Ward, A. A. Puretzky, C. M. Rouleau, Z. Gai, L. Liang, V. Meunier, B. G. Sumpter *et al.*, J. Mater. Chem. C **4**, 315 (2016).
[20] G. Lin, H. Zhuang, X. Luo, B. Liu, F. Chen, J. Yan, Y. Sun, J. Zhou, W. Lu, P. Tong *et al.*, Phys. Rev. B **95**, 245212 (2017).
[21] H. L. Zhuang, Y. Xie, P. R. C. Kent, and P. Ganesh, Phys. Rev. B **92**, 035407 (2015).
[22] S. Tongay, S. S. Varnoosfaderani, B. R. Appleton, J. Wu, and A. F. Hebard, Appl. Phys. Lett. **101**, 123105 (2012).
[23] S. Yang, C. Wang, H. Sahin, H. Chen, Y. Li, S.-S. Li, A. Suslu, F. M. Peeters, Q. Liu, J. Li *et al.*, Nano Lett. **15**, 1660 (2015).
[24] M. N. Ali, J. Xiong, S. Flynn, J. Tao, Q. D. Gibson, L. M. Schoop, T. Liang, N. Haldolaarachchige, M. Hirschberger, N. Ong *et al.*, Nature (London) **514**, 205 (2014).
[25] L. Casto, A. Clune, M. Yokosuk, J. Musfeldt, T. Williams, H. Zhuang, M.-W. Lin, K. Xiao, R. Hennig, B. Sales *et al.*, APL Mater. **3**, 041515 (2015).
[26] X. Chen, J. Qi, and D. Shi, Phys. Lett. A **379**, 60 (2015).
[27] T. J. Williams, A. A. Aczel, M. D. Lumsden, S. E. Nagler, M. B. Stone, J.-Q. Yan, and D. Mandrus, Phys. Rev. B **92**, 144404 (2015).
[28] J. Klimeš, D. R. Bowler, and A. Michaelides, Phys. Rev. B **83**, 195131 (2011).
[29] M. Dion, H. Rydberg, E. Schröder, D. C. Langreth, and B. I. Lundqvist, Phys. Rev. Lett. **92**, 246401 (2004).
[30] H. Ji, R. Stokes, L. Alegria, E. Blomberg, M. Tanatar, A. Reijnders, L. Schoop, T. Liang, R. Prozorov, K. Burch *et al.*, J. Appl. Phys. **114**, 114907 (2013).
[31] Y. Tian, M. J. Gray, H. Ji, R. Cava, and K. S. Burch, 2D Mater. **3**, 025035 (2016).